M.T. Lemmon[1], D. Toledo[2], V. Apestigue[2], I. Arruego[2], M.J. Wolff[1], P. Patel[3,4], S. Guzewich[5], A. Colaprete[6], Á. Vicente-Retortillo[7], L. Tamppari[3], F. Montmessin[8], M. de la Torre Juarez[3], J. Maki[3], T. McConnochie[1], A. Brown[9], J.F. Bell III[10]

[1]Space Science Institute, Boulder, CO 80301, USA. [2]Instituto Nacional de Técnica Aerospacial, Madrid, Spain. [3]Jet Propulsion Laboratory, California Institute of Technology, Pasadena, CA, USA. [4]Mullard Space Science Laboratory, University College London, UK. [5]NASA Goddard Space Flight Center, Greenbelt, MD, USA. [6]NASA Ames Research Center, Moffett Field, 94035, CA, USA. [7]Centro de Astrobiología (INTA-CSIC), Madrid, Spain. [8]LATMOS, Paris, France. [9]Plancius Research, MD, USA. [10]Arizona State University, Tempe, AZ, USA.

Corresponding author: Mark Lemmon (mlemmon@spacescience.org)

Key Points:

- A 22°-radius halo around the Sun was imaged for over 3 hours by cameras on the Perseverance rover at Jezero crater on Mars.
- Such a halo is diagnostic of scattering by large, hexagonal water-ice crystals and has not previously been seen off Earth.
- The halo implies that high supersaturation of water may be more common in late summer in the northern subtropics than elsewhere.

Abstract

Observations by several cameras on the Perseverance rover showed a 22° scattering halo around the Sun over several hours on the morning of sol 292 (15 December 2021). Such a halo has not previously been seen off Earth. The halo occurred during the aphelion cloud belt season and the cloudiest time yet observed from the Perseverance site. The halo required crystalline water-ice cloud particles in the form of hexagonal columns large enough for refraction to be significant, at least 11 µm in diameter and length. Near 44 km altitude, fall speeds would have been 0.3-1 m/s for the smallest allowed particles. Over the 3.3-hour duration of the halo, particles could have fallen 3-12 km, causing downward transport of water and dust. Halo-forming clouds are likely rare due to the high supersaturation of water that is required but may be more common in northern subtropical regions during mid-northern summer.

Plain Language Summary

A scattering halo, or bright ring around the Sun, was seen in pictures taken by cameras on the Perseverance rover. Such halos are commonly seen in ice clouds on Earth, but have never before been seen on Mars. When the halo was seen, on 15 December 2021, the rover was within a period of unusually cloudy weather near the end of a season known for water-ice clouds in northern tropical areas such as the rover's site in Jezero crater. The appearance and size of the halo showed that the clouds were made of water-ice crystals shaped like hexagonal columns. The crystals were likely larger than those in most water ice clouds on Mars, which allowed the halo to form.

1 Introduction

Water-ice clouds are common in Mars' northern tropics around aphelion, comprising 3- to 4-µm radius particles (Clancy et al., 2003) that have been modeled as complex polyhedra that resemble precursors of terrestrial cirrus cloud particles (Wolff et al., 2019). Terrestrial ice clouds typically develop further into an assortment of hexagonal columns and plates, along with aggregates and more complex shapes (Bailey and Hallet, 2008). Terrestrial clouds can produce a wide variety of halos, including those caused by refraction through faces inclined 60° and 90° to one another in crystals that can be randomly or preferentially oriented (Minnaert, 1974). The most common terrestrial halo is at 22° from the Sun and is caused by randomly oriented hexagonal columns (prisms) and rosettes (clusters of hexagonal prisms) in which the refraction is through faces inclined at 60° (Barran, 2009). Due to the near-Sun geometry, this halo is inaccessible to orbiting spacecraft; no halos have been reported in images by landers on other worlds.

There has been little evidence that Martian cloud particles make the transition to hexagonal prisms or attain sizes such that refraction could produce a halo. Whiteway et al. (2009) found fall streaks seen by the Phoenix LIDAR to be consistent with 42x127 µm water-ice columns, but no halos were reported in Phoenix images despite frequent clouds. This may mean that the large particles were not common, or they were irregular and did not include the necessary prism. Cooper et al. (2019, 2020) used Curiosity rover images and Mars Color Imager (MARCI) data to suggest the presence of columns. In the case of the Curiosity images, the determination was based on the statistics of radiance differences as clouds moved in the sky—there was no halo imaged—and included 20°-50° scattering angles. While no halo feature was detected in the retrieved phase function, the columnar shape was argued based on the absence of features corresponding to other shapes at larger angles. In the case of the MARCI data, the orbital geometry limited the observations to non-halo angles and the determination was also based on the absence of features from the alternative particles considered. While Cooper et al. (2020) considered aphelion cloud belt (ACB) particles to be 2.75-µm radius, no size constraint was presented.

The Perseverance rover landed in Jezero crater at 77.5°E longitude, 18.4°N latitude on 18 February 2021. In this work we show that water ice halos were visible on one or a few sols (Martian days of 24.7 hours) near the end of the rover's first year on Mars, requiring the existence of previously unexpected large, crystalline particles. In section 2, we describe imaging campaigns undertaken with Perseverance cameras and the methods by which we analyzed the data. In section 3, we report on images of a halo by three instruments, comprising four separate cameras, and discuss the implications. Section 4 summarizes conclusions.

2 Data and Methods

2.1 Imaging campaigns

Several instruments on the Perseverance rover have been used for routine reconnaissance of the environment. Cameras involved in the halo detection are Navcam, Mastcam-Z, and Skycam. The first two reside on the rover's remote sensing mast, which aims them, while the last resides on the rover's deck and is always aimed upward.

Navcam is an engineering camera designed to support rover navigation (Maki et el. 2020). It has a 96°x72° field of view (FOV) with a 5120x3840 pixel array using a Bayer pattern of microfilters to provide red, green, and blue (RGB) color images. Navcam images can be subsampled by color or position on the array and can be reduced in size by pixel summing. The images used in this study were commanded as 1280x960 RGB images spanning the full left-eye field of view; the resulting images were combined into a single file and JPEG compressed to achieve a typical transmitted-image size of 150 kB. The Navcam cloud survey campaign used 5 images to acquire a nearly full sky mosaic on several sols.

Mastcam-Z is a multispectral and stereo camera designed for geologic and atmospheric science (Bell et al. 2021). Each camera, left and right, has a variable FOV depending on the zoom setting of 26-110 mm. The sensor has a 1600x1200 array of pixels using a Bayer pattern of microfilters to provide color when using an infrared-blocking filter. For monitoring atmospheric optical depth, subframed solar images at 26- and 110-mm zoom were acquired using neutral density (ND) filters together with an IR-blocking filter for RGB images at 480, 544, and 630 nm (left camera); and a narrow 880-nm filter (right camera). To constrain aerosol properties, sky images were acquired using the full FOV of 25.6°x19.2° at 26-mm zoom. All images used here were either originally acquired with lossless compression or were re-acquired from camera memory using lossless compression.

Skycam is part of the Mars Environmental Dynamics Analyzer (MEDA, Rodriguez-Manfredi et al. 2021). It has a 1024x1024 pixel array containing a 126°-diameter FOV using fisheye optics and a circular baffle. It acquires monochrome images with an effective wavelength of 691 nm. A ND annulus on the camera window allows sky imaging while also allowing unsaturated solar imaging in mid-morning and mid-afternoon. Skycam images taken while the Sun was within the ND annulus were used to systematically track diurnal variation of optical depth and look for transient features in the sky. While Skycam images could be used for aerosol properties, we have not investigated corrections for scattering by dust on the window, which has been exposed to the Martian environment and near horizontal since landing.

2.2 Optical depth

The use of solar images to determine atmospheric optical depth followed the template described in Lemmon et al. (2015, 2019): the images were calibrated to radiance on sensor; a synthetic aperture was defined around the Sun for photometric measurements of flux; the flux was converted to normal optical depth using the estimated top-of-atmosphere flux for each sensor along with the specific image geometry.

For Mastcam-Z, Hayes et al. (2021) described the instrument calibration. For optical depth processing, the RGB images were separated to the three colors, each of which was treated separately; this resulted in four total measurements from each image pair. As with previous cameras, the ability to image at different times of day was used for a Beer-Lambert law fit, which determined what each band would have been for a hypothetical no-optical-depth case. The fit was done using mean radiance of the solar disk, to account for the varying Mars-Sun distance. No temperature corrections were needed, as these were included in the calibration, and no variability of dust on the optics was observed. See also Bell et al. (in review).

For Skycam, Rodriguez-Manfredi et al. (2021) describe the instrument calibration. The optical depth processing could not use the Beer-Lambert law relative calibration due to the limited geometry of Sun images. Rather, all close occurrences of Skycam and Mastcam-Z optical depth measurements were used to determine the top-of-atmosphere flux required for Skycam to reproduce the Mastcam-Z measurements. That value has not showed a significant trend during the mission. See also Rodriguez-Manfredi et al. (in review).

2.3 Image processing

Perseverance image headers contain geometric information sufficient to determine the pointing of each pixel, subject to the rover's attitude uncertainty. That uncertainty was near 0.5°, based on the scatter in position of the Sun in Mastcam-Z images aimed at the Sun. Mosaics of images calibrated to radiance were used for inspection and modeling. Mosaics of ratio images were used to look for time-variable features. In addition, time-variable features were identified after dividing out a smooth sky radiance profile determined by a regression of the natural logarithm of radiance that was second order in scattering angle and cosine of the zenith angle.

2.4 Radiative transfer modeling

Radiative-transfer models were performed using DISORT (Stamnes et al 1988). Baseline aerosol phase functions were prescribed using the Tomasko et al. (1999) parameterization, after correction for a size error identified by Wolff et al. (2006). In specific cases described below, a parameterized halo was added, and a Levenberg-Marquardt technique (Markwardt 2008) was used to fit the model to the data. The halo model included an inner edge (near 22°), an amplitude, a fall-off to large scattering angles, and a broadening of a few degrees.

3 Results

3.1 Sol 292 halos

A Navcam cloud survey at 08:57-09:01 local true solar time (LTST) on sol 292 (15 December 2021) showed an apparent ring around the Sun in the 3 out of 5 images that were aimed near the Sun (Fig 1). We identified the ring, which was visible in unprocessed raw images, as a candidate water-ice halo based on its scattering angle of approximately 22°. We initiated a campaign to attempt to repeat the halo image or identify it as an artifact; observations in support of this were undertaken on sols 299, 303, 304, and 308. The timing of the campaign was significantly impacted by the cadence of multi-sol weekend and pre-holiday planning. No halo was identified in the follow-up imaging in either Navcam or the supporting Mastcam-Z images.

The follow-up imaging was nonetheless useful in that several Navcam surveys were taken with nearly identical geometry to the sol 292 survey and no halo-like artifacts were seen. (No preceding survey was taken with similar geometry, given the dependence on both time of day and the rover's orientation). Figure 1 shows the ratio of the sol-292 survey to the sol-299 survey: the halo stands out clearly; other artifacts are present, but not halo-like; the image to the southeast was underexposed systematically, and thus shows more noise. While the camera has shown many arcuate and streak-like artifacts depending on the specific position of the Sun: (1) none have resembled the sol 292 images; (2) three images with different geometries showed a halo on sol 292; and (3) several surveys that repeated the sol-292 geometries did not show a halo or similar artifacts (see also Figs. S1-S2). Thus, we conclude that the feature observed on sol 292 was a real scattering feature in the Martian sky.

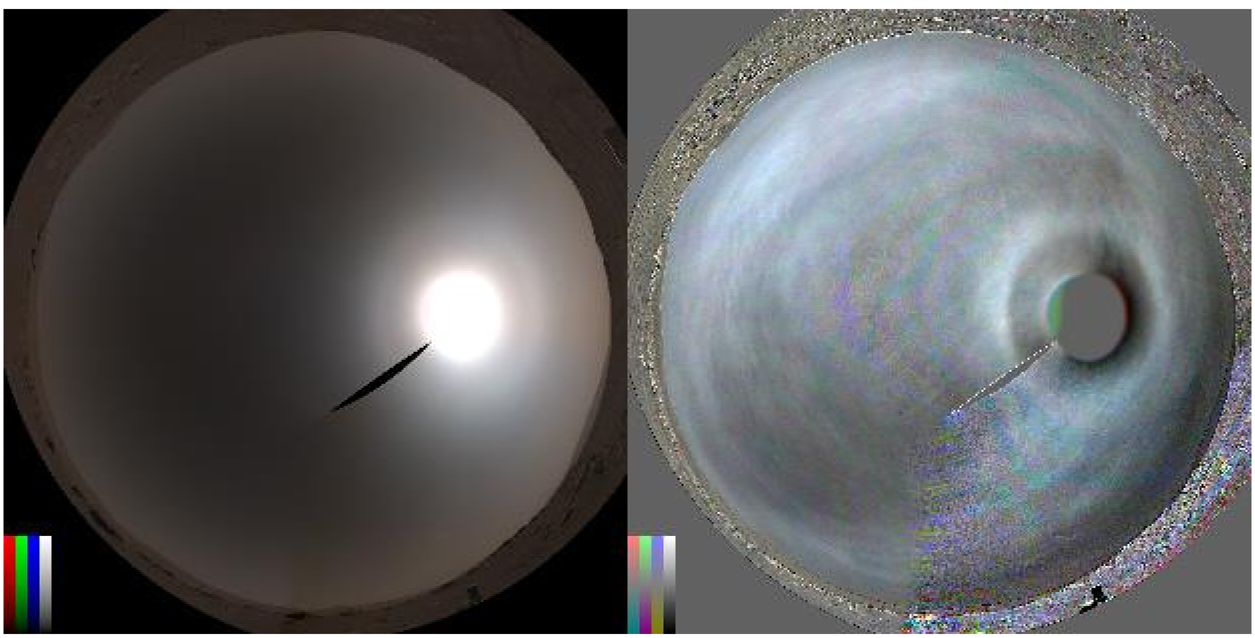

Figure 1. The sol 292 Navcam sky panorama is shown in equidistant projection (north at top, east to the right, zenith centered) on the left, and the ratio of sol 292 to 299 is shown on the right. Color-bars show radiance of 0 to 0.3 (left) and

contrast of -20% to 20% (right).

In a review of other available data from sol 292, we determined that halos could be seen in both Mastcam-Z and Skycam (Fig. 2). The only Mastcam-Z morning sky images between sols 290 and 299 were on sol 292 at 11:26 LTST. Figure 2 shows the 440- and 860-nm images in equidistant (fisheye) projection as ratio images that have a low-frequency polynomial fit divided out. A bright feature with inner edge near 22° is evident in each of the Mastcam-Z left and right cameras.

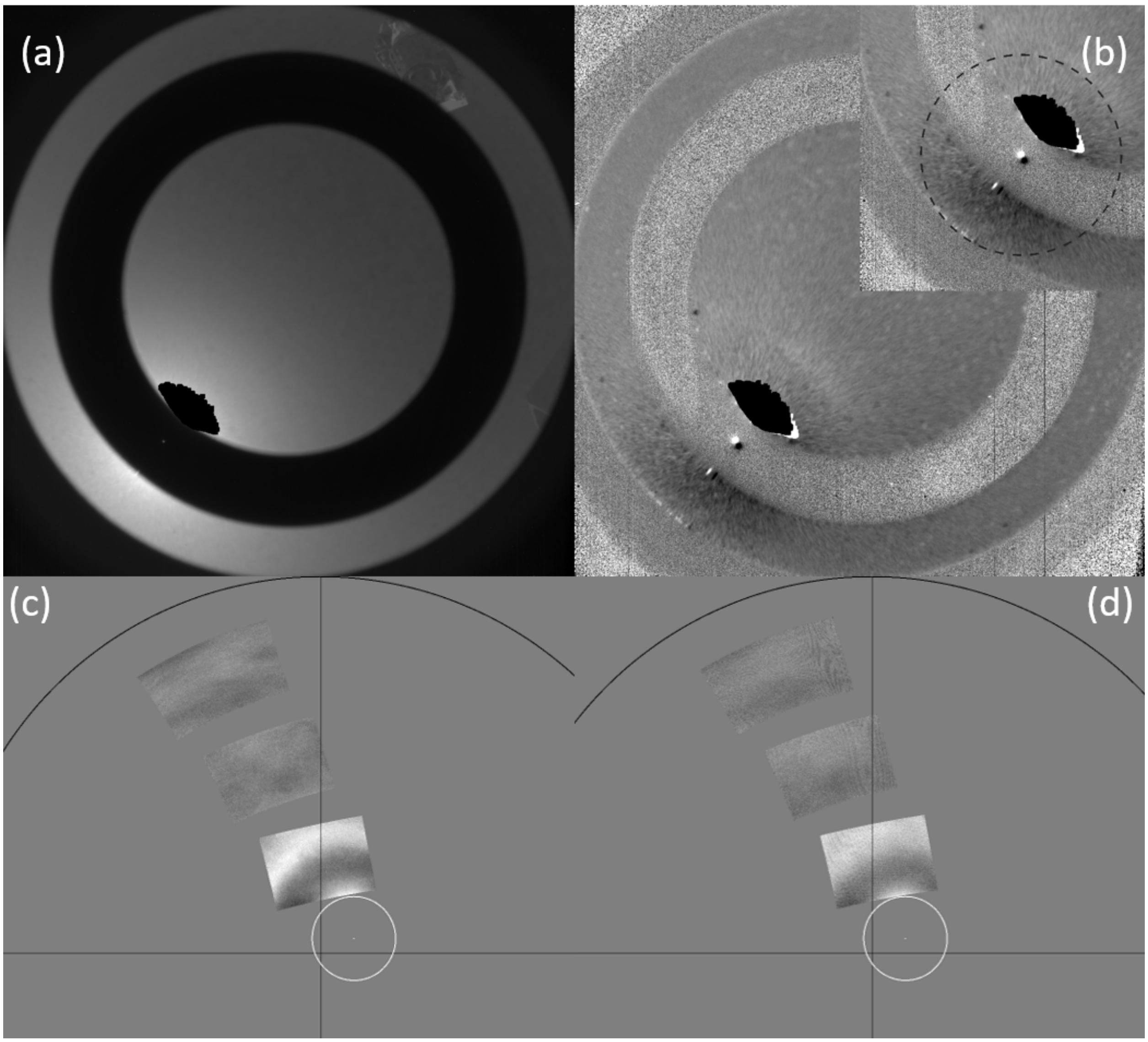

Figure 2. Skycam image for morning of sol 292 (a) with ratio to sol 299 (b). The inset in (b) shows the near-Sun quadrant with a 22° radius circle around the Sun. The halo fragment is above the Sun. Sol 292 Mastcam-Z images using the L6 (442 nm) filter (c) and the R2 (866 nm) filter (d) are shown in equidistant projection after dividing out a model background, with the horizon and N-S and E-W lines shown in black. The Sun is centered in the 10° white circles.

Skycam images were acquired regularly in the mornings at 08:34 LTST. While no halo is visible in the unprocessed image, the ratio with the sol-299 image shows an arcuate feature above the Sun (Fig. 2). We do not find the image (ratio) by itself to be sufficient evidence to demonstrate there are halos on Mars. However, given the presence of a halo that morning, we do find the image convincing that the halo was likely present as early as 08:34 LTST. A Skycam image at 14:33 LTST was the only image that sol with appropriate geometry that did not show a halo.

The MEDA Radiation and Dust Sensor (RDS) includes not just Skycam but also a series of photodiodes that take data at 1-Hz while MEDA is operating (Rodriguez-Manfredi et al. 2021; Apestigue et al. 2022). The RDS Lateral-4 sensor was looking 20° (with a 5° FOV) above the rover deck and 24° from the Sun at 08:23 LTST and showed a peak in brightness, relative to other sols (see also Figs. S3-S4).

3.2 Context

Morning ice hazes of optical depth ~0.1 were common through the Perseverance mission through sol 275, which represents solar longitudes (L_S) of 6° to 134°, or northern spring and early summer (Bell et al., in review; Rodriguez-Manfredi et al., in review). Much of this period overlapped with activity of the ACB (Tamppari et al., 2000; Wolff et al., 2019). Like at other landing sites (Lemmon et al. 2015, 2019), optical depth had declined toward a typical mid-summer (post-aphelion) minimum (Bell et al., in review). Discrete clouds were rare, but occurred in some periods (Bell et al., in review).

Around sols 280-285 (L_S 136°-139°), column optical depth started to become larger and variable at all times of day (Fig. 3). The rising trend continued through the mid-290s (sol 292 was L_S 142°), while occasional low values near 0.3 remained. Midday and afternoon optical depth returned to low values around sol 300 (L_S 147°), with morning values following by sol 305. Clouds were commonly observed in sky images and near-horizon parts of landscape images over sols 280-300 (see Fig. S5).

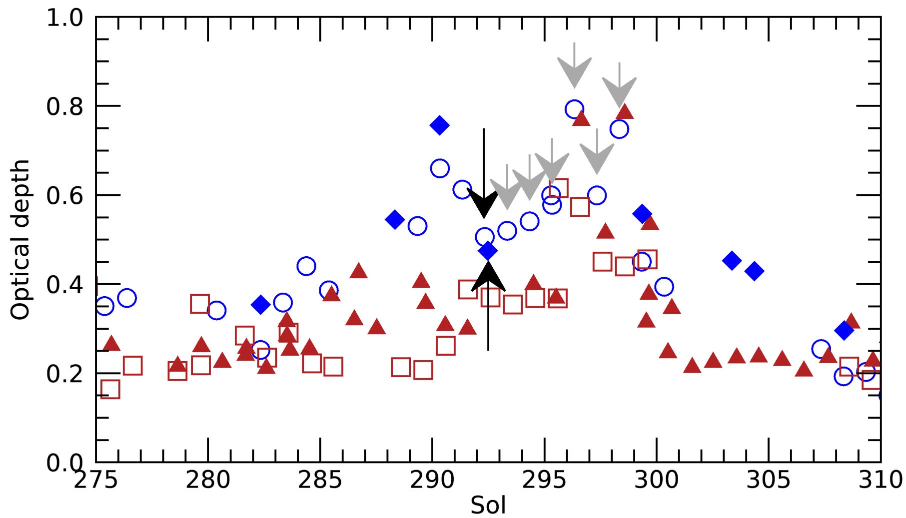

Figure 3. Column optical depth is shown for Skycam (open symbols, squares for afternoon and circles for before noon) and Mastcam-Z green channel (filled symbols, triangles for after noon and diamonds for before noon). Arrows indicate halo observations (black for sol 292, gray for possible other Skycam detections).

Pre-dawn RDS zenith photometry on sol 292 showed an anomalous sky brightening with the Sun several degrees below the horizon (see also Figs S6-S7). This brightening at high solar zenith angles (~94°) indicated the presence of a cloud layer at altitudes of ~44 km. We analyzed measurements at 450 and 950 nm with a Monte-Carlo radiative transfer code in spherical geometry and found cloud particles with radii >3 µm, suggesting a composition of water ice based on similar optical depth at 950 nm and 450 nm. We note that the data do not rule out additional clouds at lower altitudes with correspondingly slower settling velocities. At Gale crater, high-altitude, morning clouds have been estimated to move from 30-45 km altitude to >40 km altitude over L_S 120°-150°, while geometric techniques were used to measure cloud altitudes from 16.9 to 54.9 km over L_S 135°-142° (Campbell et al. 2020).

The halo-forming region was likely of order 100s of km in extent. At any moment, the lateral extent of the ice-cloud must have been 2-3 times the altitude of the clouds to form a complete halo. The 3.3-hour duration of the halo implies an extent of one to a few hundred km for realistic wind speeds.

3.3 Other candidate halos

We found no compelling halo candidates in Navcam images other than on sol 292. Mastcam-Z sky images on sols 257 (12:51 LTST) and 258 (12:06 LTST) may show more subtle halos. Halos were not found above the few percent detection level in most other Mastcam-Z sky images at 22° scattering angle. Some Mastcam-Z images have reflection artifacts that may or may not be masking a halo. Skycam images around 08:30 LTST on sols 293-298 show weaker halo-like features than on sol 292 (Fig. S2).

In addition to the 22°-halo, water ice has a halo at 46° and carbon dioxide ice has halos at 26° and 39° (Cowley and Schroeder, 1999). None of these halos were identified in the images with the 22° halo or other images in this period. Both cloud compositions can produce other optical effects, none of which were observed.

3.4 Implications for Martian clouds

Halos are geometric-optics (refraction) features that do not exist for cloud particles small compared to wavelength and thus the presence of halos sets a lower limit for particle size. Bi and Yang (2014) showed T-Matrix calculations of the transition for compact prisms with length (L) of twice the size of a hexagon facet (so, L ~ D, diameter). They found that the halos emerged and then became insensitive to size over the size parameter (2 L/ , where is wavelength) range of 80 to 150. For green light, that is L of 7 to 13 µm; at 866 nm, that is 11 to 21 µm. Thus, we estimate 11 µm to be the minimum length and diameter. A 46° halo is more prominent for plates ($L<D$) and less prominent for columns ($L>D$). For arbitrarily large particles, surface roughness degrades or eliminates the halos (Yang et al. 2008). Thus, we do not consider the halo to be diagnostic of size above the minimum allowed value.

The inner edge of the geometric-optics halo varies with wavelength due to the changing index of refraction of water and is at 21.7° and 22.5° for red and blue light. Halos can be smoothed by both diffraction (for small particles) and roughness, such that the peak brightness can be outside 22° by an amount depending on the smoothing. Figure 4 shows the observed and model data for the 442- and 866-nm images. The best fit had an inner edge at 23.5° and 21.9°, with smoothing of 3°-4°, but the edge angles are likely uncertain by ~1-2°. Contrast from Skycam (691 nm) and Navcam (630, 540, and 480 nm) ratio images (see Figs 1-2) are also shown in Fig. 4. The fits' inner edges were at 21.1°, 22.9°, 23.0°, and 23.2°. Apparent smoothing declined from 1.3° to 0.6° with decreasing wavelength, roughly consistent with diffraction of a sharp edge with a 40- to 60-µm scale. The later Mastcam-Z images seemed to require larger smoothing, consistent with 8- to 9-µm diffraction scales, but which could instead relate to roughness or aggregation.

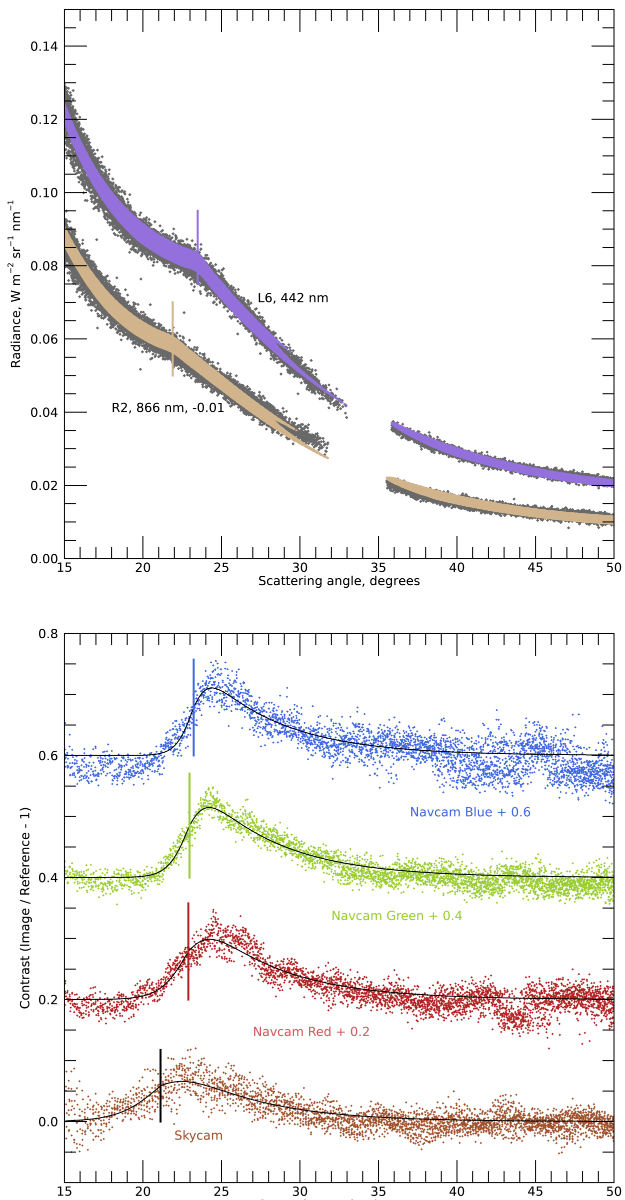

Figure 4. Halo brightness versus scattering angle. (a) Mastcam-Z radiance values are shown in dark gray for L6 and R2 (lower curve, offset -0.01) with models (purple and tan) and vertical lines indicating the best fit angle of the halo's inner edge. (b) From bottom: fractional residuals are shown for Skycam (tan) and Navcam red, green, and blue channels using sky above the Sun in sol 292 vs. 299 ratio images. Each has a superposed model halo shape and vertical

line indicating the best fit angle of the halo's inner edge.

For terrestrial clouds at low temperatures (-75 °C < T <-40 °C), columns and rosettes form at high ice supersaturation (>20%), while lower supersaturation (1-2% up to 10-15%) results in irregular crystals and complex polyhedra (Bailey and Hallet, 2008). In Martian conditions, heterogeneous nucleation (growth on condensation nuclei such as the abundant dust) of water ice requires supersaturation above around 18% (Määttänen et al. 2005). Nucleation rate increases exponentially with increasing supersaturation up to around 100%. Thus, it is likely that the particles that formed the halo grew in a higher-supersaturation environment than non-halo-forming clouds. A plausible mechanism is cooling from thermal tides, which could have a vertical extent of a scale height, and which may have interacted with gravity waves to produce a supercooled region of several km vertical scale. Alternatively, at a given rate, total ice volume increases proportionate to time spent in the supersaturated region, so a paucity of dust condensation nuclei coupled with a long period of growth might also produce sufficiently large particles. The relative efficiency of high supersaturation makes that our preferred hypothesis.

To form a halo of ~10% contrast, we estimate that >1% of the optical depth must be halo-forming ice. A much larger fraction, with a much lower-contrast halo (i.e., due to diffraction or roughness) is permitted. For sol 292, the minimum large-crystalline optical depth was 0.005, requiring as little as ~0.03 Pr-µm (precipitable-microns) of water ice in the form of 11-µm columns. Total ice optical depth was 0.1-0.3, requiring no more than 2-5 Pr-µm of water ice for 11- to 30-µm columns in the absence of opacity from smaller particles. Ice optical depth was higher (0.4-0.6) on sol 296; this could also have been of order 1 Pr-µm if it comprised only ~3-µm particles.

The absence of prior halo detections may relate to the climatology of the ACB. No other landers have been as deep within the ACB: the larger, "Type 2" ice clouds of Clancy et al. (2003) occur from L_S 30°-140° at latitudes 0°-25°N. While there were two possible halos earlier, the sol-292 halo detection was in an unusually cloudy phase at the end of ACB season. It is possible that halos could be seen once to several times annually at Perseverance's latitude but are rare to nonexistent at the other sites. It remains unclear why halos were not seen during the Phoenix mission.

Ice sedimentation within halo-forming clouds impacts the vertical distribution of both water and dust. We estimated settling velocities of between 0.3 and 1 m s^{-1}--or timescales of a few hours--to fall one scale height near 40-50 km altitude. Particle radii greater than 5 µm implies a dust vertical transport by cloud scavenging of about 10 km in a few hours, leading to dust clearing at the altitudes where the nucleation takes place. By reducing the abundance of condensation nuclei and radiative heating by dust, one halo event may increase the likelihood of halos near the temperature minimum of nearby sols.

4 Conclusions

We provide the first report of an optical (scattering) halo on another planet, in this case a 22° halo caused by water ice. We show that on sol 292 of the Perseverance mission, a halo was observable over a 3.3-hour period of mid- to late-morning. The halo was detected by 4 cameras at 6 wavelengths. The halo, along with possible detections on the subsequent 6 sols, occurred during a cloudy and icy period that lasted from sols 285-300, during the aphelion cloud belt season. Two possible earlier halos were also associated with cloudy weather. The presence of a halo implied crystalline water-ice particles grew to >11 µm in length and diameter as hexagonal prisms (columns). Associated meteorological data suggested that the clouds started near 44 km altitude, although they could have precipitated by several km to more than a scale height during the morning. Halo-forming clouds are likely rare due to the high supersaturation of water that is required but may be more common in northern subtropical regions during mid-northern summer.

Acknowledgments

The authors acknowledge and profusely thank the Mars 2020 team from its conception through assembly through operations on Mars. Funding for the U.S.-based authors of this work was provided by the National Aeronautics and Space Administration's Mars 2020 Project, either directly or via subcontracts from the California Institute of Technology's Jet Propulsion Laboratory and Arizona State University. Funding for Spain-based co-authors was provided by the Spanish Ministry of Economy and Competitiveness, through the projects No. ESP2014-54256-C4-1-R (also -2-R, -3-R and -4-R) and AYA2015-65041-P; Ministry of Science, Innovation and Universities, projects No. ESP2016-79612-C3-1-R (also -2-R and -3-R), ESP2016-80320-C2-1-R, RTI2018-098728-B-C31 (also -C32 and -C33) and RTI2018-099825-B-C31; Instituto Nacional de Técnica Aeroespacial; Ministry of Science and Innovation's Centre for the Development of Industrial Technology; Grupos Gobierno Vasco IT1366-19; and European Research Council Consolidator Grant no 818602. A. V.-R. is supported by the Spanish State Research Agency (AEI) Project No. MDM-2017-0737 Unidad de Excelencia "María de Maeztu"- Centro de Astrobiología (INTA-CSIC). The authors declare that they have no competing interests.

Open Research

All Perseverance data used in this study are publicly available via the Planetary Data System. The subset of Mastcam-Z products used here include a sequence ID of ZCAM01xxx. The subset of Navcam products used here include a sequence ID of NCAM00501. The sol range is defined in the text and all data files include a 4-digit sol in the filename.

Mastcam-Z: Bell, James F.; Maki, Justin M. (2021). Mars 2020 Mast Camera Zoom Bundle, from Arizona State University Mastcam-Z Instrument Team, calibrated products. PDS Imaging Node. DOI: 10.17189/q3ts-c749.

MEDA: Rodriguez-Manfredi, Jose A; de la Torre Juarez, Manuel (2021). Mars 2020 Perseverance Rover Mars Environmental Dynamics Analyzer (MEDA) Experiment Data Record (EDR) and Reduced Data Record (RDR) Data Products Archive Bundle. PDS Atmospheres Node. DOI: 10.17189/1522849.

Navcam: Maki, Justin M. (2021). Calibrated data products for the Mars 2020 Perseverance Rover Navigation Cameras. PDS Imaging Node. DOI: 10.17189/yvkm-rx37.

References

Apestigue, V., A. Gonzalo, J.J. Jimenez, J. Boland, M. Lemmon, J.R. de Mingo, E. Garcia-Menendez, J. Rivas, J. Azcue, L. Bastide, N. Andres-Santiuste, J. Martinez-Oter, M. Gonzalez-Guerrero, A. Martin-Ortega, D. Toledo, F.J. Alvarez-Rios, F. Serrano, B. Martin-Vodopivec, J. Manzano, R. Lopez-Heredero, I. Carrasco, S. Aparicio, Á.Carretero, D.R. MacDonald, L.B. Moore, M. Ángeles Alcacera, J.A. Fernández-Viguri, I. Martín, M. Yela, M. Álvarez, P. Manzano, J.A. Martín, J.C. del Hoyo, M. Reina, R. Urqui, J.A. Rodriguez-Manfredi, M. de la Torre Juárez, C. Hernandez, E. Cordoba, R. Leiter, A. Thompson, S. Madsen, M.D. Smith, D. Viúdez-Moreiras, A. Saiz-Lopez, A. Sánchez-Lavega, L. Gomez-Martín, G.M. Martínez, F.J. Gómez-Elvira, and I. Arruego, 2022. Radiation and Dust Sensor for Mars Environmental Dynamic Analyzer onboard M2020 Rover. *Sensors* **2022**, 22(8), 2907, DOI:10.3390/s22082907.

Bailey, M.P., and J. Hallet (2008). A comprehensive habit diagram fore atmospheric ice crystals: Confirmation from the laboratory, AIRS II, and other field studies. *J. Atmos Sci.* **66**, 2888-2899. DOI: 10.1175/2009JAS2883.1.

Barran A.J. (2009). A review of light scattering properties of cirrus. *J. Quant. Spectroscopy and Radiative Transfer* **110**, 1239-1260. DOI: 10.1016/j.jqsrt.02.026.

Bell, J.F., III, J.N. Maki, G.L. Mehall, M.A. Ravine, M.A. Caplinger, Z.J. Bailey, S. Brylow, J.A. Schaffner, K.M. Kinch, M.B. Madsen, A. Winhold, A.G. Hayes, P. Corlies, C. Tate5 · M. Barrington, E. Cisneros, E. Jensen, K. Paris, K. Crawford, C. Rojas, L. Mehall, J. Joseph, J.B. Proton, N. Cluff, R.G. Deen, B. Betts, E. Cloutis, A.J. Coates, A. Colaprete, K.S. Edgett, B.L. Ehlmann, S. Fagents, J.P. Grotzinger, C. Hardgrove, K.E. Herkenhoff, B. Horgan, R. Jaumann, J.R. Johnson, M. Lemmon, G. Paar, M. Caballo-Perucha, S. Gupta, C. Traxler, F. Preusker, M.S. Rice, M.S. Robinson, N. Schmitz, R. Sullivan, and M.J. Wolff (2021). The Mars 2020 Perseverance Rover Mast Camera Zoom (Mastcam-Z) Multispectral, Stereoscopic Imaging Investigation. *Space Science Reviews*, **217**, 24. DOI: 10.1007/s11214-020-00755-x.

Bell III, J.F., J.N. Maki, S. Alwmark, B.L. Ehlmann, S.A. Fagents, J.P. Grotzinger, S. Gupta, A. Hayes, K.E. Herkenhoff, B.H. N. Horgan, J.R. Johnson, K.B. Kinch, M.T. Lemmon, M.B. Madsen, J.I. Núñez, G. Paar, M.a Rice, J.W. Rice Jr., N. Schmitz, R. Sullivan, A. Vaughan, M.J. Wolff, A. Bechtold, T. Bosak, L.E. Duflot, A.G. Fairén, B. Garczynski, R. Jaumann, M. Merusi, C. Million, E. Ravanis, D.L. Shuster, J. Simon, M. St. Clair, C. Tate, S. Walter, B. Weiss, A. Bailey, T. Bertrand, O. Beyssac, A. Brown,

P. Caballo-Perucha, M.A. Caplinger, C.M. Caudill, F. Cary, E. Cisneros, E. Cloutis, N. Cluff, P. Corlies, K. Crawford, S. Curtis, R. Deen, D. Dixon, C. Donaldson, M. Barrington, M. Ficht, S. Fleron, M. Hansen, D. Harker, R. Howson, J. Huggett, S. Jacob, E. Jensen, O.B. Jensen, M. Jodhpurkar, J. Joseph, C. Juarez, L.C. Kah, M. Kanine, J. Kristensen, T. Kubacki, K. Lapo, A. Magee, M. Maimone, G.L. Mehall, L. Mehall, J. Mollerup, D. Viúdez-Moreiras, K. Paris, K. Powell, F. Preusker, J. Proton, C. Rojas, D. Sallurday, K. Saxton, E. Scheller, C.H. Seeger, M. Starr, N. Stein, N. Turenne, J. Van Beek, A.G. Winhold, R. Yingling. Geological and Meteorological Imaging Results from the Mars 2020 Perseverance Rover in Jezero Crater. In review.

Bi, L., and P. Yang (2014). Accurate simulation of the optical properties of atmospheric ice crystals with the invariant imbedding T-matrix method. *J. Quant. Spectroscopy and Radiative Transfer* **138**, 17-35. DOI: 10.1016/j.jqsrt.2014.01.013.

Campbell. C., S. Guzewich, C. Smith, J. Kloos, M. Lemmon, C.A. Moore, B. Cooper, R. Haberle, and J. Moores (2020). Estimating the Altitudes of Martian Water-Ice Clouds Above the Mars Science Laboratory Rover Landing Site. *Planet. Space Sci.,* **182**, 104785. DOI: 10.1016/j.pss.2019.104785

Clancy, R.T., M.J. Wolff, and P.R. Christensen (2003). Mars aerosol studies with the MGS TES emission phase function observations: Optical depths, particle sizes, and ice cloud types versus latitude and solar longitude. *J. Geophys. Res.* **108** (E9), 5098. DOI: 10.1029/2003JE002508.

Cooper, B.A., J.E. Moores, D.J. Ellison, J.L. Kloos, C.L. Smith, S.D.Guzewich, and C.L. Campbell (2019). Constraints on Mars Aphelion Cloud Belt phase function and ice crystal geometries. *Planet. Space Sci.* **168**, 62-72. DOI: 10.1016/j.pss.2019.01.005.

Cooper, B.A., J.E. Moores, J.M. Battalio, S.D. Guzewich, C.L. Smith, R.C.N. Modestino, and M.V. Tabascio (2020). Aphelion Cloud Belt phase function investigations with Mars Color Imager (MARCI). *Planet. Space Sci.* **184**, 104840. DOI: 10.1016/j.pss.2020.104840.

Cowley, L., and M. Schroeder (1999). Forecasting Martian halos. *Sky & Telescope*, December 1999, pp. 60-64.

Hayes, A.G., P. Corlies, C. Tate, M. Barrington, J.F. Bell, J.N. Maki, M. Caplinger, M. Ravine, K.M. Kinch, K. Herkenhoff, B. Horgan, J. Johnson, M. Lemmon, G. Paar, M.S. Rice, E. , T.M. Kubacki, E., R. Deen, B.L. Ehlmann, E. Lakdawalla, R. Sullivan, A. Winhold, A. Parkinson, Z. Bailey, J. van Beek, P. Caballo-Perucha, E. Cisneros, D. Dixon, C. , O.B. Jensen, J. Kuik, K. Lapo, A. Magee, M. Merusi, J. Mollerup, N. Scudder, C. Seeger, E. Stanish, M. Starr, M. Thompson, N. Turenne, and K. Winchell (2021) Pre-Flight Calibration of the Mars 2020 Rover Mastcam Zoom (Mastcam-Z) Multispectral, Stereoscopic Imager. *Space Science Reviews* **217**, 29. DOI: 10.1007/s11214-021-00795-x

Lemmon, M.T., M.J. Wolff, J.F. Bell III, M.D. Smith, B. Cantor, and P.H.

Smith (2015). Dust aerosol, clouds, and the atmospheric optical depth record over 5 Mars years of the Mars Exploration Rover mission. *Icarus* **251**, 96-111. DOI: 10.1016/j.icarus.2014.03.029.

Lemmon, M.T., S. D. Guzewich, T. McConnochie, A. de Vicente-Retortillo, G. Martinez, M.D. Smith, J. F. Bell III, D. Wellington, and S. Jacob (2019). Large dust aerosol sizes seen during the 2018 Martian global dust event by the Curiosity rover. *Geophys. Res. Lett.* **46**, 9448-9456. DOI: 10.1029/2019GL084407.

Määttänen, A., H. Vehkamäki, A. Lauri, S. Merikallio, J. Kauhanen, H. Savijärvi, and M. Kulmala (2005). Nucleation studies in the Martian atmosphere. *J. Geophys. Res.* **110**, E02002. DOI: 10.1029/2004JE002308.

Maki. J.N., D. Gruel, C. McKinney, M.A. Ravine, M. Morales, D. Lee, R. Willson, D. Copley-Woods, M. Valvo, T. Goodsall, J. McGuire, R.G. Sellar, J.A. Schaffner, M.A. Caplinger, J.M. Shamah, A.E. Johnson, H. Ansari, K. Singh, T. Litwin, R. Deen, A. Culver, N. Ruoff, D. Petrizzo, D. Kessler, C. Basset, T. Estlin, F. Alibay, A. Nelessen, and S. Algermissen1 (2020). The Mars 2020 Engineering Cameras and Microphone on the Perseverance Rover: A Next-Generation Imaging System for Mars Exploration. *Space Sci. Rev.* **216**, 137. DOI: 10.1007/s11214-020-00765-9.

Markwardt, C.B. (2008). Non-linear least squares fitting in IDL with MPFIT. Astronomical Data Analysis Software and Systems XVII A.16. ASP Conference Series, Vol. XXX, 2008. J. Lewis, R. Argyle, P. Bunclarck, D. Evans, and E. Gonzales-Solares, eds.

Minnaert, M.G.J. (1974). Light and color in the outdoors. Translated and revised by L. Seymour (1993). Springer, New York, NY, USA.

Rodriguez-Manfredi, J.A., M. de la Torre Juárez, A. Alonso, V. Apéstigue, I. Arruego, T. Atienza, D. Banfield, J. Boland, M.A. Carrera, L. Castañer, J. Ceballos, H. Chen-Chen, A. Cobos, P.G. Conrad, E. Cordoba, T. del Río-Gaztelurrutia, A. de Vicente-Retortillo, M. Domínguez-Pumar, S. Espejo, A.G. Fairen, A. Fernández-Palma, R. Ferrándiz, F. Ferri, E. Fischer, A. García-Manchado, M. García-Villadangos, M. Genzer, S. Giménez, J. Gómez-Elvira, F. Gómez, S.D. Guzewich, A.-M. Harri, C.D. Hernández, M. Hieta, R. Hueso, I. Jaakonaho, J.J. Jiménez, V. Jiménez, A. Larman, R. Leiter, A. Lepinette, M.T. Lemmon, G. López, S.N. Madsen, T. Mäkinen, M. Marín, J. Martín-Soler, G. Martínez, A. Molina, L. Mora-Sotomayor, J.F. Moreno-Álvarez, S. Navarro, C.E. Newman, C. Ortega, M.C. Parrondo, V. Peinado, A. Peña, I. Pérez-Grande, S. Pérez-Hoyos, J. Pla-García, J. Polkko, M. Postigo, O. Prieto-Ballesteros, S.C.R. Rafkin, M. Ramos, M.I. Richardson, J. Romeral, C. Romero, K.D. Runyon, A. Saiz-Lopez, A. Sánchez-Lavega, I. Sard, J.T. Schofield, E. Sebastian, M.D. Smith, R.J. Sullivan, L.K. Tamppari, A.D. Thompson, D. Toledo, F. Torrero, J. Torres, R. Urquí, T. Velasco, D. Viúdez-Moreiras, S. Zurita, and the MEDA team (2021). The Mars Environmental Dynamics Analyzer, MEDA. A suite of environmental sensors for the Mars 2020 mission. *Space Sci. Rev.* **217**, 48. DOI: 0.1007/s11214-021-00816-9.

Rodriguez-Manfredi, J.A., et al. (in review). The rich meteorology of Jezero crater over the first 250 sols of Perseverance on Mars. In review.

Stamnes, K., S-C. Tsay, W. Wiscombe, and K. Jayaweera (1988). *Applied Optics* **27**, 2502-2509.

Tamppari, L.K., R.W. Zurek, and D.A. Paige (2000). Viking era water-ice clouds. *J. Geophys. Res.* **105** (E2), 4087-4107. DOI: 10.1029/1999JE001133.

Tomasko, M.G., L.R. Doose, M.T. Lemmon, P.H. Smith, and E. Wegryn 1999. Properties of dust in the martian atmosphere from the Imager for Mars Pathfinder. *J. Geophys. Res.*, **104**, 8987-9007, doi: 10.1029/1998JE900016.

Whiteway, J.A., L. Komguem, C. Dickinson, C. Cook, M. Illnicki, J. Seabrook, V. Popovici, T. J. Duck, R. Davy, P. A. Taylor, J. Pathak, D. Fisher, A. I. Carswell, M. Daly, V. Hipkin, A.P. Zent, M.H. Hecht, S.E. Wood, L. Tamppari, N. Renno, J. Moores, M.T. Lemmon, F. Daerden, P.H. Smith, 2009. Mars Water Ice Clouds and Precipitation. *Science* **325**, 68-70. doi: 10.1126/science.1172344.

Wolff, M.J., M.D. Smith, R.T. Clancy, N. Spanovich, B.A. Whitney, M.T. Lemmon, J. Bandfield, D. Banfield, A. Ghosh, G. Landis, P. Christensen, J.F. Bell III, and S. Squyres, 2006. Atmospheric results from Mars Global Surveyor overflights of the Mars Exploration Rovers. *J. Geophys. Res.* **111**, E12S17, doi: 10.1029/2006JE002786.

Wolff, M.J., R.T. Clancy, M.A Kahre, R.M. Haberle, F. Forget, B.A. Cantor, and M.C. Malin (2019). Mapping water ice clouds on Mars with MRO/MARCI. *Icarus* **332**, 24-49. DOI: 10.1016/j.icarus.2019.05.041.

Yang, P., G. Hong, G.W. Kattawar, P. Minnis, and Y. Hu (2008). Uncertainties associated with the surface texture of ice particles in satellite-based retrieval of cirrus clouds: Part II—Effect of particle surface roughness on retrieved cloud optical thickness and effective particle size. *IEEE Trans. Geosci. and Remote Sensing* **46**, 1948-1957. DOI: 10.1109/TGRS.2008.916472.